Microscopic Characterisation of Photo Detectors from CMS Hadron Calorimeter

R A Shukla,[1] V G Achanta,[1] P D Barbaro,[2] S R Dugad,[1, a)] A Heering,[3] S K Gupta,[1] I Mirza,[1] S S Prabhu,[1] and P Rumerio[4, 5]

[1)] *Tata Institute of Fundamental Research, Mumbai, India*

[2)] *University of Rochester, New York, USA*

[3)] *University of Notre Dame, Indiana, USA*

[4)] *University of Alabama, Tuscaloosa, Alabama, USA*

[5)] *CERN, Geneva, Switzerland*

(Dated: 27 June 2018)

The CMS hadron Calorimeter is made of alternating layers of scintillating tiles and metals, such as brass or iron. The original photo detectors were hybrid units with a single accelerating gap called Hybrid Photo Diodes (HPD). Scintillating light was transmitted to the HPDs by means of optical fibers. During data taking at the Large Hadron Collider (LHC), the signal strength of scintillator tiles of detector units in the forward region degraded significantly due to the damage related to the amount of radiation to which the scintillator was exposed to. Scintillators suffer damage when exposed to radiation, however, the amount of damage observed was more than originally estimated. Several HPDs were removed during a detector shut down period. Microscopic scans of relative quantum efficiencies for few of these HPDs were made. The damage of the photocathode was determined to vary with the amount of optical signal transmitted by optical fibers to the HPD. Imprints of each fiber (~ 1 mm) on the photocathode with varying damage within the same pixel were observed. Most of the observed reduction of the calorimeter signal can be attributed to localised damage of the photocathode.

I. INTRODUCTION

The CMS Hadron Calorimeter[1] is designed to accurately measure the energy of jets produced in proton-proton (pp) collisions. The calorimeter consists of different sub-detectors, a) Barrel (HB[2,3]), b) Endcap (HE[4]), c) Outer Barrel (HO[5,6]) and d) Forward (HF[7]). The HB, HE, and HO sub-detectors are sampling calorimeters and use scintillator embedded with wavelength shifting fibers (WLS) as an active element. In the HE and HB detectors, there are several layers of scintillators interleaved with an absorber. The detector is segmented in fine $\eta - \phi$ towers, where η represents the pseudorapidity of a tower, defined as,

$$\eta = -ln(tan(\theta/2)) \tag{1}$$

where θ is the polar angle of a tower *w.r.t.* the pp collision axis and ϕ represents the azimuth angle of tower in the detector. The size of tower defined in $\eta - \phi$ direction is typically about 0.087×0.087 radians. Wavelength-shifting (WLS) fibers spliced to a clear optical fiber are used to transport the scintillation light to the photo-readout elements[8]. The optical fibers from several sampling layers within the same $\eta - \phi$ tower are grouped together inside an *Optical Decoding Unit* (ODU) and are mapped onto a designated pixel on the HPD. Another fiber, also coupled to the HPD, brings light produced by an LED, for calibration purposes. Customised Hybrid Photo Diodes (HPDs) manufactured

by DEP[9] were installed as photo-readout elements[10–12] for these detectors. They have high gain, immunity to magnetic field when aligned to HPD axis[13] and a compact size. Each HPD has a hexagonal shape with common photocathode and 19 isolated photodiodes underneath, referred to as pixels (p-i-n pixels). The HPDs were designed to operate for 10 years in the CMS experiment, corresponding to an integrated charge of 3 C/pixel at the highest pseudo-rapidity locations[14]. The HPDs have a hexagonal shape. Figure 1(a) shows a schematic representation of an HPD. The geometry of the HE detector is shown in Fig. 1(c). As can be seen, there are several layers of scintillators in each $\eta - \phi$ tower. Towers with higher η-index are closer to beam pipe, and scintillator layers at shallower depth (lower layer number) in a given tower are closer to the pp collision point. Hence, layers with higher η index and lower depth are expected to produce higher scintillation light. The mapping of HE towers on to the pixels of an HPD is shown in Fig. 1(b).

Gradual degradation in the light output of HE detector with increasing integrated luminosity has been observed since its operation. Some degradation is expected, due to the presence of very high radiation in this region, up to $\approx$ 0.2 Mrad during LHC Run 1, which may cause damage to either the scintillator or the HPDs or both. In-situ studies of the radiation damage to this detector are carried out using LED, radioactive source calibration, and collision data itself. Though these studies have shown significant degradation in the overall performance of the detector, they do not have the ability to decouple radiation damage to the scintillators from damage to the HPDs due to integrated use. Recently, some HPDs from the HE and HO detectors were removed, to carry out an independent
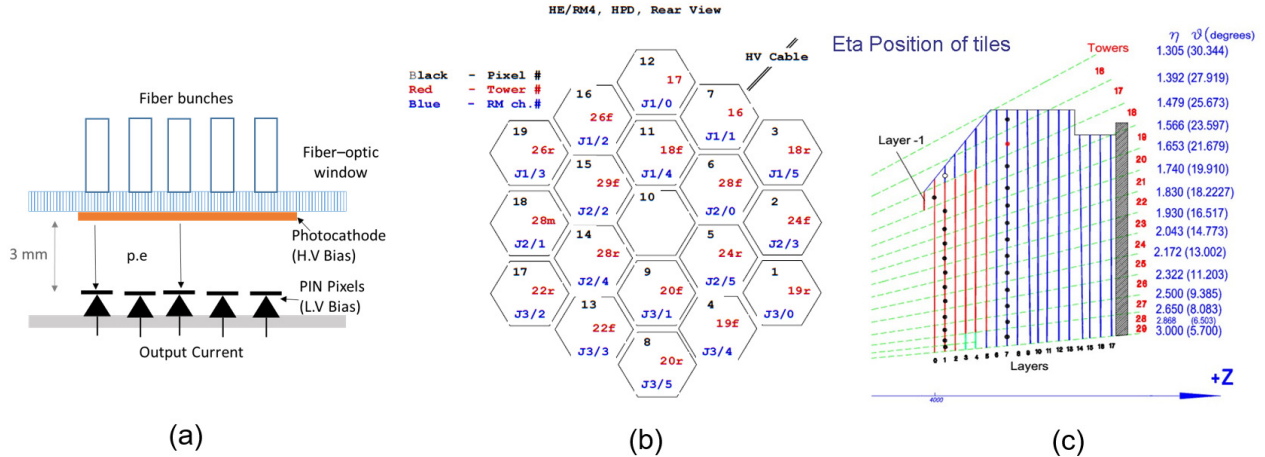
———————

a)Electronic mail: dugad@cern.ch

FIG. 1.   a) Schematic of the design of HPD; b) Typical mapping of HE towers onto an HPD. The number on each pixel represents the pixel number within the HPD, the geometrical tower number and the electronics index on the readout card; and c) Geometrical schematic of the towers in the HE detector.

study of the cumulative effect on them. Since, HPDs are primarily exposed to green light from the scintillator, the response of the decommissioned HPDs to green light (λ=520 nm) was studied using the *Micron Resolution Optical Scanner* (MROS), which was specially designed and built for microscopic characterisation of photo detectors such as silicon photo-multipliers[15]. The MROS has been demonstrated to provide a focused beam of light on a target. The detector under test in this setup can be moved in an automated manner in three orthogonal directions with a step size of 0.1 μm. Using this setup, an extensive microscopic characterisation of the HPDs obtained from the HO and HE detectors has been carried out. These studies have revealed significant localised damage to the photocathode of the HPD decommissioned from the HE detector, whereas the damage observed for the HO HPD is quite small and restricted to light incident by the calibration fiber on photocathode. Details of the experimental methods used and results that have been obtained are discussed in the following sections.

II.   EXPERIMENTAL SETUP

The design of the MROS[15] is quite suitable for a fine scan of HPD. The device under test (HPD) is mounted on a motion table consisting of three linear stages capable of motion in three orthogonal directions with a resolution of 0.1 μm and with a dynamic range of 25 mm. Size of the common photocathode of an HPD is also about 25 mm, thus, almost the entire surface area of the device can be scanned. The recorded localised photo response at each scanning position yields complete map of the device response across its photocathode. For ease of measurement and integration, the HPD mounting board was modified to provide the sum of all PIN diode currents (rather than 19 individual currents) into the ammeter. The detailed electrical connection diagram is shown in Fig. 2. Since the MROS would illuminate an ultra-fine spot on a pixel selectively, while other pixels

are in the dark, the net output current can still be attributed to a scanned position on the particular pixel. The MROS also has a built-in imaging capability, which helps in carrying out a visual inspection of the surface of the detector, as well as in selecting a particular region of interest to be scanned. It is to be noted that the laser intensity is kept low during the scan to avoid any possible damage of the photocathode during long runs. The overall experimental setup is shown in Fig. 3.
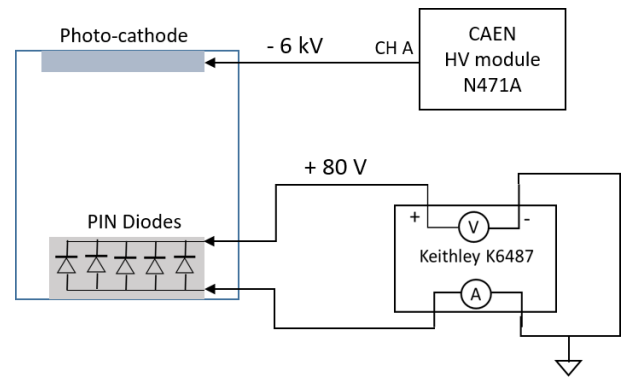

FIG. 2. Electrical connections of the HPD module with Bias Voltage for PIN diodes and High Voltage for the photocathode.

An HPD requires two power supplies for its operation. As shown in Fig. 2, a high voltage (negative) bias is applied to the photocathode to accelerate the photoexcited electrons emitted by the photocathode (photon energy $E_\gamma \geq$ work function of photocathode). All photo-diodes are connected in parallel for this study. A common low voltage (80 Volts) is applied across all the diodes to adequately reverse bias them. As can be seen from Fig. 3, photo-diodes are placed at the anode region of the vacuum tube. The high energy electrons impinging on the photo-diode give rise to a large number of carriers which are further multiplied and efficiently transported (less scattering and recombination) to the output electrode
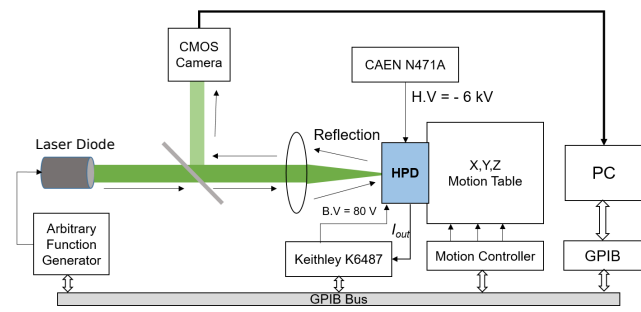
FIG. 3. Experimental setup for microscopic characterisation of an HPD.

due to the presence of the diode bias (electric field). Thus, such a combined arrangement yields a large gain of about 2000 with low noise. The high cathode voltage at which the energy of the accelerated electrons become sufficient to generate detectable current inside photo-diode is referred to as the breakdown voltage of the HPD; beyond this voltage the output current increases linearly with over voltage (difference between applied and breakdown voltage). Typical I-V characteristics of the photocathode (illuminated with laser light) with constant photo-diode bias voltage (BV = 80 Volts) is shown in Fig. 4. The breakdown voltage plays an important role in the overall operation of the HPD and is discussed in detail in Section V.
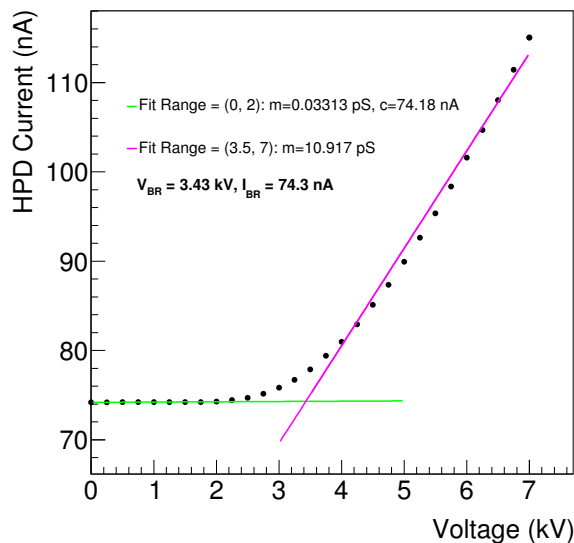

FIG. 4. I-V characteristic of the HPD photocathode under constant illumination and a constant photodiode bias of 80 Volts.

III.   IMAGING AND FOCAL AXIS DETERMINATION

Before an HPD can be microscopically scanned, a built-in CMOS camera system was used to survey the surface of the device and access the scan area. The imaging also helps in roughly determining the focal plane position i.e aligning HPD surface to the focal plane. Figure 5

shows a typical image of an HPD surface taken with the built-in CMOS camera. The square array pattern is a typical characteristic of the fiber optic plate (FOP) of the HPD. The FOP is an optical device comprised of a bundle of micron-diameter optical fibers. The FOP directly conveys light incident on its input surface to its output surface. A modified knife-edge method was adapted to accurately determine the position of the focal plane and to establish the laser beam profile on the photocathode with the fiber optic window.
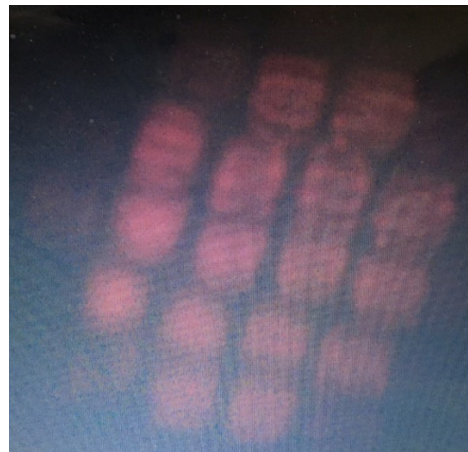

FIG. 5. Image of the HPD surface recorded with the built-in CMOS camera.

A.   Knife-edge Measurement

In a typical knife-edge method[15,16], a sharp-edged object is placed in the light beam path between a focusing lens and a detector (e.g a PIN diode). The knife-edge is moved perpendicular to the beam direction in fine steps, cutting it across and simultaneously recording the PIN diode current to record the integrated light falling on its surface at each step. The knife edge eventually completely blocks the beam, and the PIN output falls to the typical dark current level. The recorded PIN diode current as a function of the vertical position of the knife-edge represents an integrated light intensity at each point, and hence, when differentiated, yields the actual beam profile (typically a Gaussian). The width of the profile (sigma) represents the beam spot size at a particular position along the beam axis. A similar exercise can be carried out to obtain the beam profile for different positions along the light beam line for the knife edge; the position with the smallest beam spot size represents the focal plane of the system. The standard knife-edge method was modified to perform the beam profiling without introducing a dedicated knife edge, using instead the HPD PIN diode edges, which act as a boundary between the HPD's dead and active regions to cut the beam. When the laser beam is completely in the dead area (outside PIN diode boundary), the observed HPD current is equal to its typical dark current. This situation is equivalent to completely blocking the optical beam. As the beam is scanned across the HPD, and

TABLE I. Focal plane positions at different knife-edge scan positions on the HPD.

| Scan Point	Focal Plane Position (mm)	
	HO HPD	HE HPD
A	10.170	10.430
E	10.160	10.440
B	10.060	10.350
F	10.060	10.370
C	10.070	10.250
G	9.950	10.240
D	10.080	10.320
H	10.060	10.300

(a)　(b)

FIG. 6. a) Schematic of the HPD, indicating the eight different knife-edge measurement positions (dotted lines) and b) Beam spot size, obtained for an HO-HPD using a 650 nm laser excitation at location C as a function of the beam axis position.

the beam slowly approaches an active area, the HPD current starts building up in response to incident light until beam is completely in the active area, resulting in saturation of the HPD current.

This method was used to characterise the laser beam profile on the photocathode and obtain focal plane position at eight different locations around the edges of the HPD as shown in Fig. 6(a). A laser beam of wavelength 650 nm was used for this purpose. Using the analysis procedure described in Ref. 15, size of laser beam spot was obtained as a function of position of the HPD along the beam axis (Fig. 6(b)). The dependence of the beam spot size on position w.r.t. focal plane is fitted with a functional form[17] given in Eqn. 2. The minima of beam spot (σ_0) indicates the profile of the beam on photocathode and position of the focal plane (z_0).

$$\sigma(z - z_0) = \sigma_0 \times \sqrt{1 + \left(\frac{\mathrm{M}^2\lambda(z - z_0)}{4\pi\sigma_0^2}\right)^2} \quad (2)$$

The size of the beam is observed to be 18.1 μm at the focal plane. Figure 5 shows image of the HPD surface taken with the built-in CMOS camera. The image shows that, the fiber optic plate has a feature size of about 5 μm. The differential intensity distribution is observed to be modulated around focal plane, since the size of the light beam becomes comparable to the feature size of FOP, thus, enhancing the estimation of measured beam width. However, note that the step size used in the 2D fine scan of HPD is much coarser than the measured size of the beam spot. Knife edge datasets were taken at eight different positions, as shown in Fig. 6(a). Larger sampling across the entire HPD area was useful in establishing the uniformity of the focal plane position, *i.e.* to determine if any tilt is present in the HPD surface due to imperfections in the mechanical mounting. Table I shows the focal plane positions recorded for a representative HO-HPD and HE-HPD. A small variation observed in the focal plane position is due to the small tilt present in the surface due to mounting imperfections. This tilt was then compensated dynamically by adjusting (instead of fixed) focal plane position at regular intervals during the 2-D scan with a weighted average of known focal plane positions obtained earlier with knife-edge method.
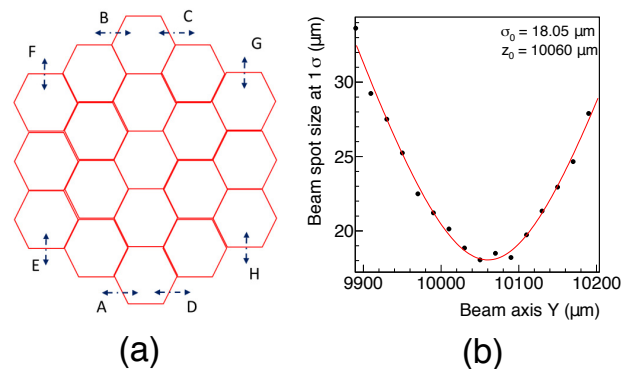
IV. 2-D SCANS

Before installing the HPDs in the CMS calorimeter, coarse 2D scans of the HPD response were done using the setup described in Ref. 14, which provided a laser beam of green light (520 nm) with beam spot size of 0.5 mm. The HPD could be moved transversely in steps of 0.5 mm. As can be seen from Fig. 7, the response of the HPD was observed to be quite uniform across the entire surface of photocathode[11]. During entire Phase-0 period of the CMS-HCAL operation, there were no HPD failures, though their performance gradually reduced with time and increasing integrated luminosity. We expect degradation in performance to increase with increasing pseudorapidity. However, at same eta, but different phi, the degradation of the signals were observed to be quite different. Since radiation damage is effectively independent of phi, the observed effect can be possibly attributed to the damage to HPDs. The HO-HPD was exposed to scintillation and calibration light at reduced high voltage (-6 kV) up to 2012 corresponding to an integrated luminosity of 6.1 fb^{-1} and 23.3 fb^{-1} at center of mass energy of 7 TeV and 8 TeV respectively. Similarly, the HE-HPD was exposed up to 2016 corresponding to an integrated luminosity of 6.1 fb^{-1}, 23.3 fb^{-1} and 45.0 fb^{-1} at center of mass energy of 7, 8 and 13 TeV respectively.

Now we present results on the microscopic characterisation of an HPD after its decommissioning from the detector. Once the focal plane positions were determined, a 2-D scan of the HPD was performed after aligning the HPD surface with the focal plane. 2-D scans were performed with a step size ranging from 200 to 300 μm to cover entire HPD area (25 mm × 25 mm), followed by finer scans with step size up to 75 μm to cover specific pixels on HPD. The HPD was raster scanned (row by row) to record the response at each predefined step to map the response. The focal axis position was dynamically adjusted every 5 mm, using the weighted average of known focal positions at different points. At each scan
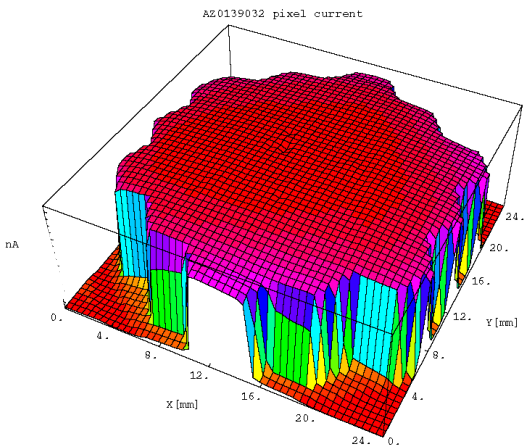
FIG. 7. 2D scan of an HPD carried out before its installation in the CMS hadron calorimeter. Figure is adapted from Ref. 11.

position (after setting up appropriate BV and HV), using laser illumination, the current flowing through the HPD was recorded as an average of 32 consecutive measurements. Dark current was recorded before starting each row by switching off the laser. Dark current measurement at the beginning of every row was necessary since the dark current was seen to have long term drift. First, an HO HPD was scanned with 650 nm laser excitation followed by 520 nm excitations. An HE HPD was scanned only with 520 nm laser. Since the spectral response of the light from the scintillator peaks at wavelengths in the green region, green laser light was used, to make the extracted information relevant.
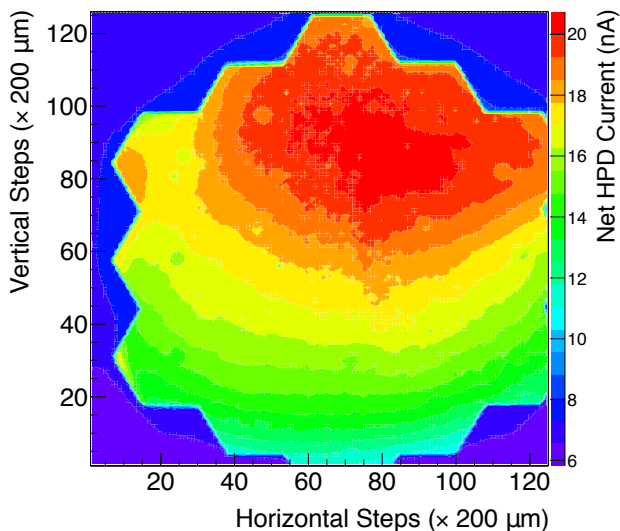
A. HO-HPD Scans

FIG. 8. Net HPD current from an HO-HPD scan recorded with 650 nm laser excitation and 200 μm step size.

Figure 8 shows the net HPD current from an HO-HPD scan recorded with 650 nm laser excitation with 200 μm

step size in the transverse direction. The scan clearly shows variation in the net HPD current across its active area. The upper right region recorded a somewhat higher current than the lower region. The dark current recorded at the beginning of each row was used to calculate the net HPD current for that row. Figure 9(a) shows the gradual variation of dark current as a function of row number. The dark current is seen to increase at the beginning of the scan. The histogram of the same is shown in Fig. 9(b). The variation in dark current during the entire run (RMS/Mean) is observed to be around 3%. Figure 9(c) shows distribution of the net HPD current in the active region. It indicates response variation of about 20% (RMS/Mean). Since the quantum efficiency of an HPD at $\lambda = 650$ nm is much lower than that for green light, the response of an HPD measured using $\lambda = 650$ nm excitation is not expected to be uniform. The 2-D scan plots also reveal faint degraded spots at certain localised regions in almost all HPD pixels. The observed localised degradation spots bring to light an interesting feature; hence, it was needed to be studied in more detail. To study these features carefully, 2-D scan of HO-HPD was performed with 520 nm laser.

Figure 10 shows the results of 2-D scans carried out with 520 nm laser excitation. As can be seen from Fig. 10(a), the response of photocathode to this wavelength is quite uniform, as compared to that observed with the 650 nm laser. The histogram of net current in the active region (Fig. 10(b)) shows a variation of about 8%. Also, faint spots seen in the 650 nm data are even more prominent in this scan due to greater sensitivity of HPD at this wavelength ($\lambda = 520$ nm). The localised degradation seems very prominent and visible in almost every pixel. This can be due to the calibration fiber installed in each pixel. Calibration runs are taken periodically by passing pulsed LED light through this fiber to monitor the gain of the HPD. Excessive illumination of localised regions of the photocathode exposed to the calibration fiber (compared to fibers coming from HO scintillators) may have led to comparatively higher degradation of photocathode under the calibration fiber area. These spots were studied in more detail with another fine scan taken around the imprint of calibration fiber with a smaller step size of 100 μm. The resulting net HPD current from the 2-D scan is shown in Fig. 11(a) while Fig. 11(b) shows a projected row scan of the same at one of the rows, passing roughly through the center of the calibration fiber imprint. A clear shadow of the size, same as that of the fiber, is seen on the photocathode. Figure 11(c) shows a histogram of the net current in a region around the shadow of fiber shown in Fig. 11(a). There are two clear gaussian distributions; the left distribution corresponds to scan points under the shadow of the calibration fiber and the right distribution corresponds to scan points outside the shadow of calibration fiber. As can be seen from this histogram, a degradation in the photon detection efficiency of about 5% (p1/p4) is observed in the photocathode area exposed to the calibration fiber w.r.t. neighbouring area. Though the reduction is not very significant, the overall setup (MROS), and the methodology adopted, demonstrates excellent sensitivity to study such
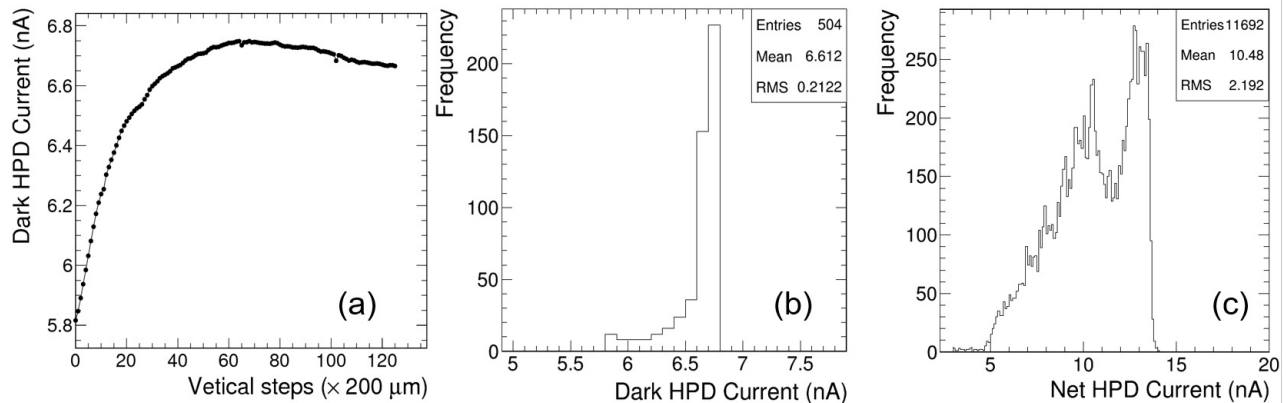
FIG. 9. a) Dark current of HPD recorded at the beginning of each scan row. b) Distribution of HPD dark current recorded at the beginning of each scan row. c) Distribution of net HPD current recorded at each scan position
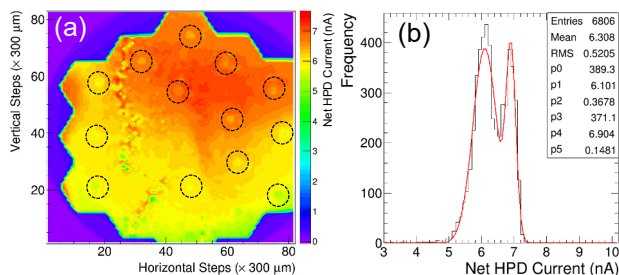

FIG. 10. An HO-HPD 2-d scan recorded with 520 nm laser excitation and 300 μm step size: a) 2-D scan of the net HPD current and b) Distribution of net HPD current recorded at each scan position.

important features of HPD response. Subsequently, similar studies were also carried out for HE HPD which have gone through substantial radiation exposure as compared to HO-HPD. These studies on the HE-HPD are discussed in the following section.

B. HE-HPD Scans

Similar to the HO HPD scans presented in the previous section, an HPD decommissioned from the HE detector (HEP17 RM4) was also scanned with a 520 nm laser beam. A 2-D scan of the entire photocathode area of an HE-HPD was recorded with a step size of 200 μm. The 2D scan of net HPD current at each scan position is shown in Fig. 12(a). The scan clearly shows many distinct features including several fiber imprints in almost every pixel of the HPD. Figure 12(b) shows a histogram of the net HPD current, indicating overall variation (RMS/Mean) of the HPD response across entire surface of photocathode to be around 17%. This is significantly larger than that observed in the HO-HPD at the same wavelength. As expected, this suggests higher overall damage of the photocathode of an HPD, extracted from the HE detector. Further, the HE-HPD scan shows the presence of many circular spots of same size as that of the fibers coming from the scintillators. They are due to

degradation of photocathode under the shadow of these fibers. This can be attributed to the higher amount of scintillation light produced by the HE scintillators due to the large radiation they receive. The resulting light, which is incident on the photocathode of the HPD, significantly damaged the region of photocathode which is under the fibers coming from scintillators. It is to be noted that the photocathode of the HO-HPD (Fig. 10) under the shadow of fibers coming from its scintillator did not show any degradation. In the HE detector, each pixel on the HPD is illuminated with a different quantity of scintillation light, depending on the location and depth of the scintillator layer in a tower. As explained above, towers with higher pseudorapidity, larger area of scintillator tile, and shallower depth are expected to produce larger scintillation light (see Fig. 1(c)). Hence, pixels mapping to such towers should see a higher degradation of the photocathode.

A pixel with a higher number of visible fiber imprints (pixel 14, tower 28R containing 13 layers of scintillators starting from layer number 5), shown by dashed circle in Fig. 12(a) was investigated further with another finer scan of the area under this pixel, recorded with step size of 75 μm. Tower 28R is closer to the beam pipe, and hence it is expected to have higher damage. As can be seen from Fig. 13(a), almost all fiber imprints (corresponding to scintillator fibers) in this pixel are clearly visible. They possess different shades, indicating varying damage, depending on the depth of the scintillator layers in this tower (see Fig. 1(c)). The degradation due to calibration fiber is not clearly visible for this HPD. Figure 13(b) shows a sectional plot (taken near row 40), which clearly shows that the photocathode area under the fibers from scintillators has been damaged significantly. The extent of the average damage for this pixel was estimated by making a histogram of the net current recorded at each scan point shown in Fig. 13(c). The histogram has two distinct distributions fitted with a Gaussian functions to extract the mean and sigma for each distribution. The left distribution corresponds to the part of the photocathode area covered by the fibers, and the right distribution shows rest of the area,
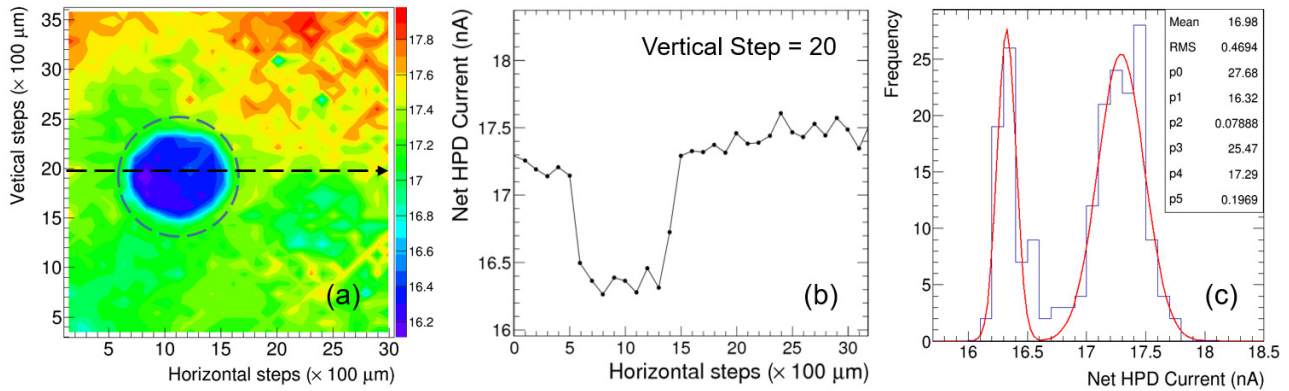
FIG. 11. a) Localised 2D fine scan of HO-HPD recorded around fiber imprint area with 520 nm laser excitation and 100 μm step size, b) Row scan passing through center of imprint (Row Number: 20) and c) Distribution of net HPD current in vicinity of the fiber spot shown in a) by dashed circle.

with no fiber cover. The ratio of peaks (p1/p4) of these two distributions shows a relative reduction in the photocathode efficiency of $\sim 46\%$. It is to be noted that this reduction is only for that area of photocathode that is exposed to fibers coming from scintillators. Variation of the response within the fiber imprint area is observed to be about 10% (p2/p1).

Due to high resolution of the scan, the same data for this pixel can also be used to deduce the layer dependence of damage for a given tower on HPD pixel. Scintillators at lower depth (smaller layer number) should cause more damage compared to those further away from the interaction region (higher layer number). Tower 28R, read by pixel 14, has 13 fibers reading scintillation light from layer numbers 5 to 17. The layer mapping of each fiber spot was done using the real optical decoder unit (ODU) used for this HPD (ODU 19.4.27 from RM4-HEP 17). Mapping of layer number to corresponding fiber spot is shown in Fig. 13(a). The average photo response of each layer was obtained by sampling those points on a row scan (passing through the center of fiber) that are within the fiber under consideration. The response of the photocathode under each fiber of each layer as a function of layer number is shown in Fig. 14. A strong correlation between the relative photocathode response and corresponding layer number can be seen from this figure. As expected, the farthest layer (L17) shows least damage and the innermost layer (L5) shows highest damage. The response of L17 is observed to be $\sim 46\%$ higher than L5. However, in order to have good jet energy resolution, all the layers should have uniform response within $\pm 5\%$. Hence, such large variation in the HPD response across different layers of the same tower affects the energy resolution of the jets produced in pp collisions that impact the HE calorimeter.

A few more fine scans, with a step size of 150 μm, were recorded around the damaged area for four other pixels mapping to different pseudorapidity towers in the HE detector. The location of the tower for each scanned pixel is obtained using Fig. 1(b) and Fig. 1(c). The 2-D scan of net HPD current for pixels 2, 6, 15 and 16

TABLE II. Summary of the local damage observed in different HE HPD pixels. Tower index is followed by depth (f: front and r: rear)

Pixel No.	No. of layers	Tower Index	pseudorapidity	Damage (%)
2	6	24f	2.17	25
16	6	26f	2.50	41
14	13	28r	2.87	54
6	3	28f	2.87	55
15	3	29f	3.00	59

are shown in Fig. 15(a) - (d). The overall degradation of each pixel is obtained using the same procedure described above. Table II shows the degradation observed in five pixels in a single HPD that map to different η towers. The measured degradation of the photocathode corresponding to each pixel confirms that the damage is larger at higher pseudorapidity regions due to higher scintillation light produced by high radiation levels, thus resulting in higher erosion of photocathode.

V. BREAKDOWN VOLTAGE UNIFORMITY

As discussed in the previous sections, several 2-D scans of HE-HPDs showed significant non-uniformity in the response of the photocathode. Degradation of the photocathode is caused by excessive illumination by scintillation light. Localised areas on the photocathode directly exposed to the scintillation light through fibers have been damaged severely, whereas other part of the photocathode, which is not exposed to the scintillation light, do not indicate any visible damage. This observation is expected to manifest as a possible variation in the breakdown voltage of the HPD, as well as a change in the I-V response, measured at damaged and normal locations on photocathode. To ascertain this, I-V characteristic of the HE-HPD was measured at all 13 damaged spots on pixel 14 (tower 28R) as well as at normal positions on the photocathode using the following procedure: a) HPD with all pixels was
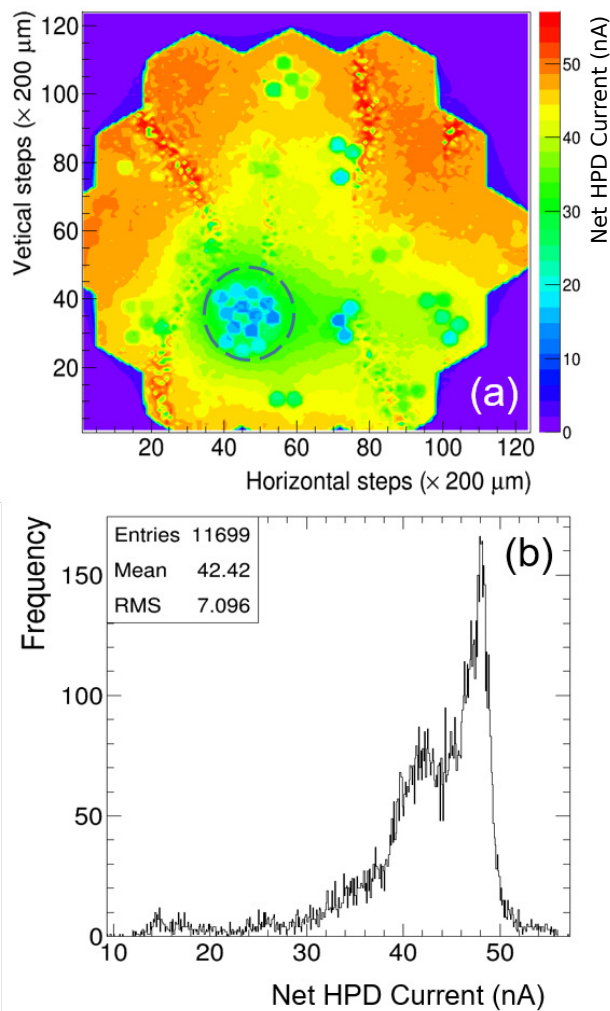
FIG. 12. a) HE-HPD 2D scan recorded with 520 nm laser excitation and 200 μm step size. b) Distribution of net HPD current recorded at each scan position.

biased with a constant BV of 80 Volts, b) predefined location was illuminated with a focused laser beam of wavelength 520 nm using the MROS setup and c) with these conditions, high voltage (HV) was ramped up from 0 to -7000 Volts in steps of 250 Volts and at each step, the HPD current was recorded. The dark current was noted by switching off the laser at the beginning of ramp up and end of ramp down cycle at each position.

Centre position of each fiber imprint on the pixel-14 of the photocathode was identified using the 2D scans taken earlier. Similarly, several positions which did not show any damage were also identified using the same data. At each of these pre-defined positions, the I-V data was taken using the procedure described above. Typical I-V characteristics is shown in Fig. 4. The breakdown voltage is obtained by taking the intersection of the lines obtained by fitting the data in two different regions (below and above the breakdown region) as shown in the same figure. The slope of second line (above the breakdown region) represents the conductance of photodiode (dI/dV) at that position. The conductance

depends on the flux of incident photoelectrons emitted by the photocathode. For the same intensity of laser, this flux is expected to be lower for lower layer number and thus should have smaller conductance. As can be seen from Fig. 16(a), the conductance, indeed, strongly depends on the layer number and follows the same trend as observed in 2D-scan of the HPD (Fig. 14). Thus, analysis of I-V data provides an independent verification of a localised damage of the photocathode that is proportional to the incident scintillation light. Figure 16(b) shows the distribution of breakdown voltage measured at normal and damaged locations. The breakdown voltage at damaged locations is observed to be about 200 Volts higher compared to that at locations with a normal photocathode. The increase in the breakdown voltage is expected due to localised thickening of the dead layer on the silicon surface.

VI. SUMMARY AND CONCLUSIONS

Independent studies of damage to HPDs used in the CMS hadron calorimeter due to excess exposure to scintillation light were important to assess its impact on the detection and measurement of the energies of jets produced in the proton-proton collisions. The Micron Resolution Optical Scanner (MROS), built for microscopic characterisation of photodetectors was leveraged for this purpose. It was suitably modified to house HPDs, as well as its associated data acquisition system. Microscopic characterisation of two HPDs, decommissioned from the HO and the HE detector, was carried out using MROS with two types of focused laser beams of 650 nm and 520 nm wavelengths. Before characterising the HPDs, the profile of the laser beam on the surface of the photocathode was carried out to establish the size of the beam spot. It was measured to be 18.1 μm, much finer than the step size (75-300 μm) used for performing the HPD scan. Subsequently, several 2-D scans were carried out with different step sizes; lower step sizes were used to study smaller regions of interest. The results of these studies presented in this article clearly demonstrate degradation of the photocathode of the HPDs from both detectors. The overall variation of the photocathode response was observed to be 8% and 17% for the HO and the HE HPD, respectively.

Moreover, several circular features in the 2D scans of net HPD current were seen for HPDs from both detectors. The diameters of these spots were the same as that of fibers carrying either scintillation light or calibration light. This clearly indicates localised damage of the photocathode in the areas directly exposed to the light coming through fibers. Though the HPD from the HO detector did not show any damage due to scintillation light, a significant localised damage of photocathode caused by excessive illumination due to scintillation light was observed in the HPD decommissioned from the HE detector. It is to be noted that the HO detector is located behind the HB detector;
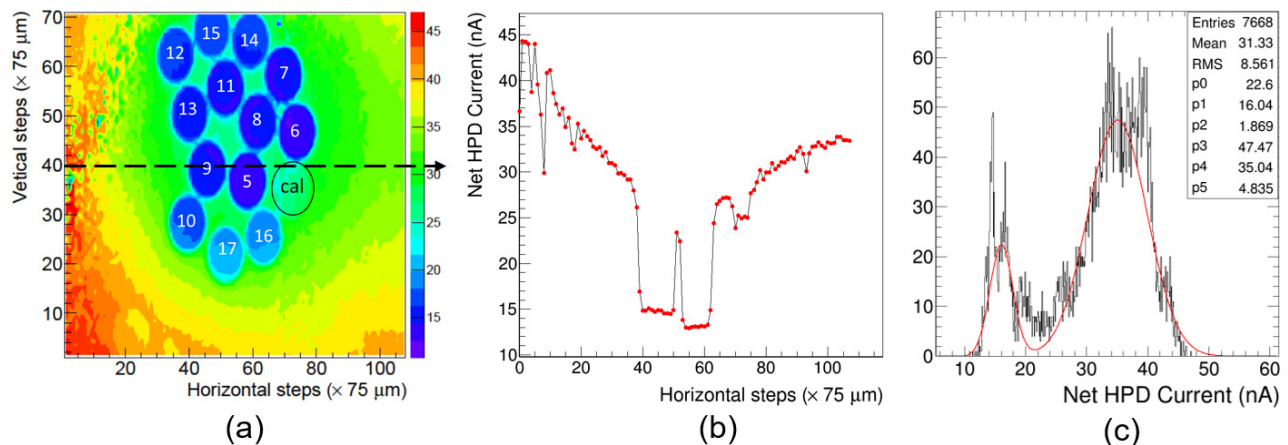
FIG. 13. a) 2D fine scan of pixel 14 of HE-HPD with 520 nm laser and 75 μm step size. Number within each fiber spot represents the layer number of that fiber. b) Sectional view of the 2D fine scan data for pixel 14 of the HE HPD. c) Distribution of net HPD current recorded at each scan position.
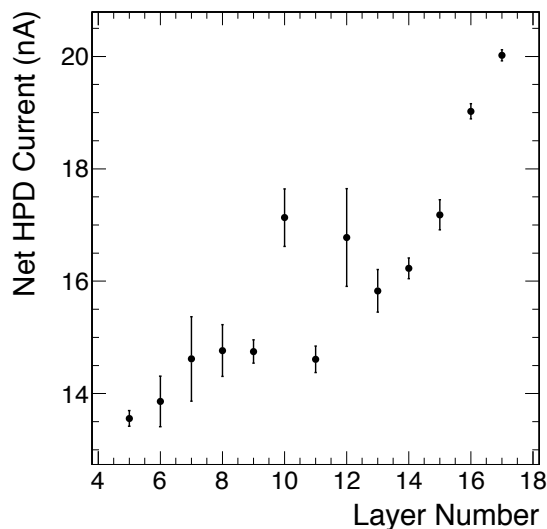

FIG. 14. Plot of net average HPD current for each fiber as a function of its layer number for Pixel 14 of the HE-HPD.

thus the fluence of charged particles through the HO scintillators is significantly smaller than that through the HE scintillators. As expected, larger damage of the photocathode was seen for those fibers collecting scintillation light from scintillators located at higher pseudorapidity and shallower depth. This region has much higher radiation generated by proton-proton collisions. Fine scans recorded around one such damaged pixel (Pixel 14, connected to tower 28R with 13 layers) show that the photocathode damage is higher for fibers originating from shallower depth scintillators (closer to the proton-proton collision point). In addition, the part of the photocathode exposed to fibers from the highest layer number registered $\sim 46\%$ higher net HPD current compared to that observed with lowest depth. In the beginning of CMS physics run, all these layers in a given tower were shown to have uniform response within $\pm 5\%$. A differential degradation of $\sim 46\%$ can significantly deteriorate the jet energy resolution of

the calorimeter. Similar fine scans for several pixels mapping different pseudorapidities were done for the HE-HPD. As expected, the damage was observed to be proportional to the pseudorapidity.

Non-uniform response of the photocathode of the HE-HPD, observed using fine photo scans with focused laser light, implies that the breakdown voltage and conductance measured at damaged and normal regions of photocathode need not be the same. Measurement revealed that, indeed, the breakdown voltage measured at the damaged region (~ 3.4 kV) is about 200 Volts higher than that measured in the normal region of photocathode. Also, the conductance was observed to be higher for higher layer numbers. The dependence of conductance on layer number (Fig. 16(a)) is quite similar to that observed in the 2D scans (Fig. 14). Hence, both the methods, that are independent of each other, confirm localised damage of photocathode proportional to the incident scintillation light.

ACKNOWLEDGMENTS

[1] "CMS: The hadron calorimeter technical design report," Tech. Rep. (1997).

[2] G. Baiatian, A. M. Sirunyan, I. Emeliantchik, V. Massolov, et al. (CMS HCAL Collaboration), "Design, Performance, and Calibration of CMS Hadron-Barrel Calorimeter Wedges," Tech. Rep. CMS-NOTE-2006-138 (CERN, Geneva, 2007).

[3] S. Abdullin, V. Abramov, B. Acharya, et al., The European Physical Journal C 55, 159 (2008).

[4] G. Baiatian, A. M. Sirunyan, I. Emeliantchik, et al. (CMS HCAL Collaboration), "Design, Performance, and Calibration of CMS
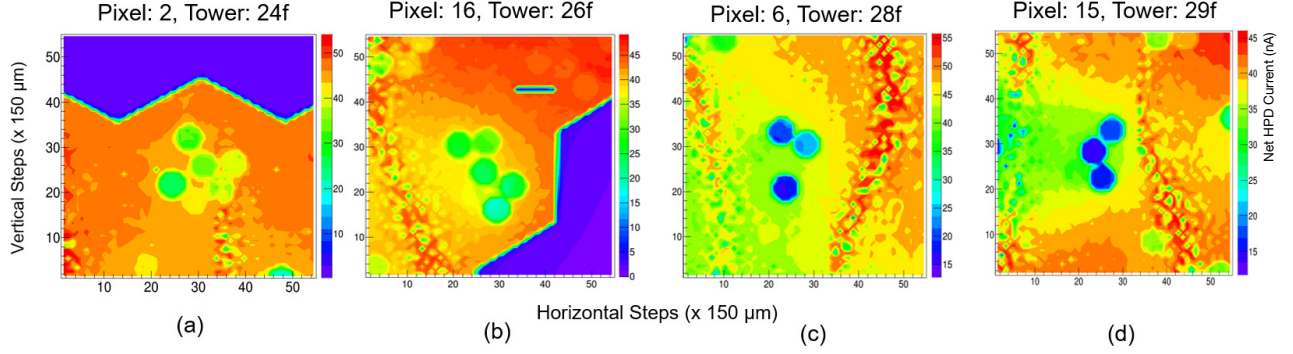
FIG. 15. 2D fine scans of the HE HPD recorded at four different pixels with laser of 520 nm excitation and step size of 150 μm
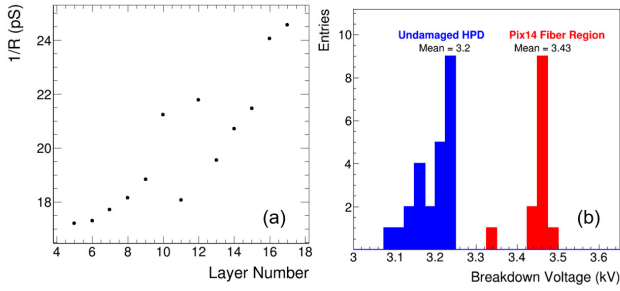

FIG. 16. a) Conductance as a function of layer number and b) Distribution of breakdown voltage for a normal (blue) and a damaged region (red) of the photocathode obtained using I-V characteristics recorded at different locations.

Hadron Endcap Calorimeters," Tech. Rep. CMS-NOTE-2008-010 (CERN, Geneva, 2008).

[5] S. Abdullin, V. Abramov, B. Acharya, *et al.*, The European Physical Journal C **57**, 653 (2008).

[6] B. S. Acharya, T. Aziz, S. Banerjee, *et al.*, "The CMS Outer Hadron Calorimeter," Tech. Rep. CMS-NOTE-2006-127 (CERN, Geneva, 2006).

[7] S. Abdullin, V. Abramov, B. Acharya, *et al.*, The European Physical Journal C **53**, 139 (2008).

[8] V. Kryshkin and A. Ronzhin, Nuclear Instruments and Meth-ods in Physics Research Section A: Accelerators, Spectrometers, Detectors and Associated Equipment **247**, 583 (1986).

[9] DEP (Delft Electronic Products), Dwazziewegen 2 Roden,9301 Netherlands.

[10] J. Elias, Nuclear Instruments and Methods in Physics Research Section A: Accelerators, Spectrometers, Detectors and Associated Equipment **387**, 104 (1997), new Developments in Photodetection.

[11] P. Cushman, A. Heering, and A. Ronzhin, *BEAUNE 1999 New Developments in Photodetection: Proceedings of the 2nd International Conference on New Developments in Photodetection (NDIP99), Beaune, France, June 21-25, 1999*, Nucl. Instrum. Meth. **A442**, 289 (2000).

[12] P. Cushman, A. Heering, J. Nelson, C. Timmermans, S. Dugad, S. Katta, and S. Tonwar, Nuclear Instruments and Methods in Physics Research Section A: Accelerators, Spectrometers, Detectors and Associated Equipment **387**, 107 (1997), new Developments in Photodetection.

[13] P. Cushman, A. Heering, and A. Ronzhin, Nuclear Instruments and Methods in Physics Research Section A: Accelerators, Spectrometers, Detectors and Associated Equipment **418**, 300 (1998).

[14] P. Cushman and B. Sherwood, "Lifetime Studies of the 19-channel Hybrid Photodiode for the CMS Hadronic Calorimeter," Tech. Rep. CMS-NOTE-2008-011 (CERN, Geneva, 2007).

[15] R. Shukla, S. Dugad, C. Garde, A. Gopal, S. Gupta, and S. Prabhu, Review of Scientific Instruments **85**, 023301 (2014).

[16] A. H. Firester, M. E. Heller, and P. Sheng, APPLIED OPTICS **16** (1977).

[17] H. Kogelnik, APPLIED OPTICS **4** (1965).